



1 **High mid-Holocene accumulation rates over West Antarctica inferred from**
2 **a pervasive ice-penetrating radar reflector**

3
4 Julien A. Bodart¹, Robert G. Bingham¹, Duncan A. Young², Joseph A. MacGregor³, David
5 W. Ashmore⁴, Enrica Quartini^{2,5}, Andrew S. Hein¹, David G. Vaughan⁶, and Donald D.
6 Blankenship²

7
8 ¹School of GeoSciences, University of Edinburgh, Edinburgh, UK

9 ²Institute for Geophysics, University of Texas at Austin, Austin, Texas, USA

10 ³Cryospheric Sciences Laboratory, NASA Goddard Space Flight Center, Greenbelt, Maryland, USA

11 ⁴School of Environmental Sciences, University of Liverpool, Liverpool, UK

12 ⁵Department of Astronomy, Cornell University, Ithaca, New York, USA

13 ⁶British Antarctic Survey, Cambridge, UK

14

15 *Correspondence to:* Julien A. Bodart (julien.bodart@ed.ac.uk)

16

17

18 **Key points**

19

- 20
- 21 • We estimate mean accumulation rates for the past ~5000 years across the Pine Island,
22 Thwaites, and Institute and Möller ice-stream catchments in West Antarctica using a
23 ubiquitous radar-sounded and ice core-dated Internal Reflecting Horizon
 - 24 • Accumulation rates were 18% higher during the mid-Holocene compared to modern rates
25 over the Amundsen-Weddell-Ross Sea divide
 - 26 • Spin-up of ice-sheet models must account for time-varying changes in accumulation rates
between the Last Glacial Maximum and the present



27 **Abstract**

28

29 Modelling the past and future evolution of the West Antarctic Ice Sheet (WAIS) to atmospheric and
30 ocean forcing is challenged by the availability and quality of observed palaeo-boundary conditions. Key
31 potential data for reconstructing past ice-sheet processes on large spatial scales are Internal Reflecting
32 Horizons (IRHs) detected by Radio-Echo Sounding (RES) techniques. When isochronal and dated at
33 ice cores, IRHs can be used to determine palaeo-accumulation rates and patterns. Using a spatially
34 extensive IRH over Pine Island Glacier, Thwaites Glacier, Institute and Möller Ice Streams, and a local
35 layer approximation model, we infer mid-Holocene accumulation rates over the slow-flowing parts of
36 these catchments for the past ~5000 years. By comparing our results with modern climate reanalysis
37 models and observational syntheses, we estimate that accumulation rates over the Amundsen-Weddell-
38 Ross divide were on average 18% higher than modern rates during the mid-Holocene. However, no
39 significant spatial changes in the accumulation pattern were observed. These higher mid-Holocene
40 accumulation-rate estimates match previous palaeo-accumulation estimates from ice-core and targeted
41 RES surveys over the ice divide, and also coincide with periods of grounding-line re-advance during
42 the Holocene over the Weddell and Ross Sea sectors. Our results highlight the need for ice-sheet models
43 to account for time-varying accumulation rates across the WAIS during the Holocene to provide better
44 estimates of its contribution to past sea-level rise.

45

46 **Key words:** West Antarctica, Internal Reflecting Horizons, Accumulation, Holocene, Ice-Penetrating
47 Radars, Ice-Core, Pine Island Glacier, Thwaites Glacier.

48



49 1. Introduction

50 Improving our knowledge of past climatic changes over the West Antarctic Ice Sheet (WAIS)
51 is required if we are to understand its present evolution and model its future under increasingly rapid
52 climatic changes (IPCC, 2021). Most studies of past ice-sheet behaviour over the WAIS have focused
53 on modelling changes in ice volume and grounding-line (GL) retreat following the Last Glacial
54 Maximum (LGM, ~20 ka Before Present, BP) (Denton and Hughes, 2002; Hillenbrand et al., 2013;
55 2014); however, less attention has been paid to ice-sheet evolution during the Holocene (~11.7 ka BP
56 to present). Recent evidence suggests that the GL may have retreated several hundred kilometres
57 inland from its current position at ~10 ka and subsequently re-advanced to reach its modern position
58 sometime during the Holocene, due to isostatic rebound and climate-induced changes, particularly
59 over the Weddell Sea and western Ross Sea sectors (Siegert et al., 2013; Bradley et al., 2015;
60 Kingslake et al., 2018; Wearing and Kingslake, 2019; Venturelli et al., 2020; Neuhaus et al., 2021;
61 Johnson et al., 2022).

62 The inland atmospheric and ice-dynamical conditions, which may have partly caused this
63 Holocene GL migration, remain relatively under-studied. An early investigation by Whillans (1976)
64 using radar data near Byrd Ice Core indicated stability during the Holocene and late Pleistocene.
65 Records of temperature and precipitation from the WAIS Divide Ice Core (hereafter abbreviated as
66 WD14; Fig. 1) in the central WAIS suggest higher accumulation rates during the Holocene than the
67 present (Fudge et al., 2016), a trend that is also observed across small parts of the Western divide
68 (hereafter referred to as WD; Fig. 1) near WD14 where isolated Radio-Echo Sounding (RES) surveys
69 have shown 15-30% higher accumulation rates during the mid-Holocene compared to modern values
70 (Siegert and Payne, 2004; Neumann et al., 2008; Koutnik et al., 2016).

71 At present, modelling studies that aim to predict future changes over the WAIS use past ice-
72 sheet reconstructions from after the LGM to guide and evaluate their models (Chavaillaz et al., 2013;
73 DeConto and Pollard, 2016; Bracegirdle et al., 2019). However, significant discrepancies between
74 model simulations and the palaeo-proxy record currently impede our ability to predict confidently
75 how the ice sheet will respond to future changes in the climate (e.g. Johnson et al., 2021). While
76 improvements in model physics and parameterisations are needed to close this gap (Bracegirdle et al.,
77 2019; Sutter et al., 2021), a considerable improvement in the availability and quality of palaeo-proxy
78 records, particularly during the Holocene, is also needed to gain a more accurate picture of the past
79 ice-sheet changes (Jones et al., 2022). Palaeo-proxy data over the WAIS have traditionally come from
80 point-based measurements, such as ice cores (WAIS Divide Project Members, 2013; Cuffey et al.,
81 2016; McConnell et al., 2017; Buizert et al., 2021), sediment cores (Hillenbrand et al., 2013; Arndt
82 et al., 2017; Hillenbrand et al., 2017; Kingslake et al., 2018; Venturelli et al., 2020; Neuhaus et al., 2021;
83 Sproson et al., 2022), or from surface-exposure dating (Stone et al., 2003; Johnson et al., 2014; Hein
84 et al., 2016; Nichols et al., 2019; Johnson et al., 2020; Braddock et al., 2022). A spatially extensive
85 alternative data source is provided by Internal Reflecting Horizons (IRHs) sounded by RES (Bingham
86 and Siegert, 2007; Harrison, 1973). When employed in combination with ice-core stratigraphy, IRHs
87 can be used to extrapolate age-depth relationships across large spatial scales by following peaks in
88 electromagnetic power in the radar data (e.g. Beem et al., 2021; Bodart et al., 2021a; Cavitte et al.,
89 2016; Jacobel and Welch, 2005; MacGregor et al., 2015; Whillans, 1976; Winter et al., 2019).

90 In comparison to East Antarctica and Greenland, extrapolating past ice-sheet records from
91 WAIS ice cores to entire glacier catchments has so far been challenging due to the limited availability
92 of deep ice cores there and, until recently, the lack of suitable datasets. However, efforts have
93 intensified in recent years to improve our understanding of the ice stratigraphy over this sector. In
94 particular, recent studies using airborne RES data over the WAIS (Karlsson et al., 2014; Muldoon et
95 al., 2018; Ashmore et al., 2020a; Bodart et al., 2021a) all identified a particularly bright IRH precisely
96 dated using the Byrd and WD14 ice-core chronologies at 4.72 ± 0.28 ka BP (Muldoon et al., 2018;



97 Bodart et al., 2021a). Comparison with volcanic sulphate deposition within the WD14 and Siple
98 Dome ice cores revealed a large peak in sulphate concentration matching the age and depth of this
99 ubiquitous layer (Kurbatov et al., 2006; Bodart et al., 2021a; Cole-Dai et al., 2021; Sigl et al., 2022),
100 which is hereafter termed the 4.72 ka IRH. This IRH has been observed by multiple RES systems
101 from different surveys and data providers. It extends through much of the slow-flowing ice of the
102 Amundsen and Weddell Sea embayments, including across the divides demarcating regions draining
103 the Amundsen, Weddell and Ross Seas.

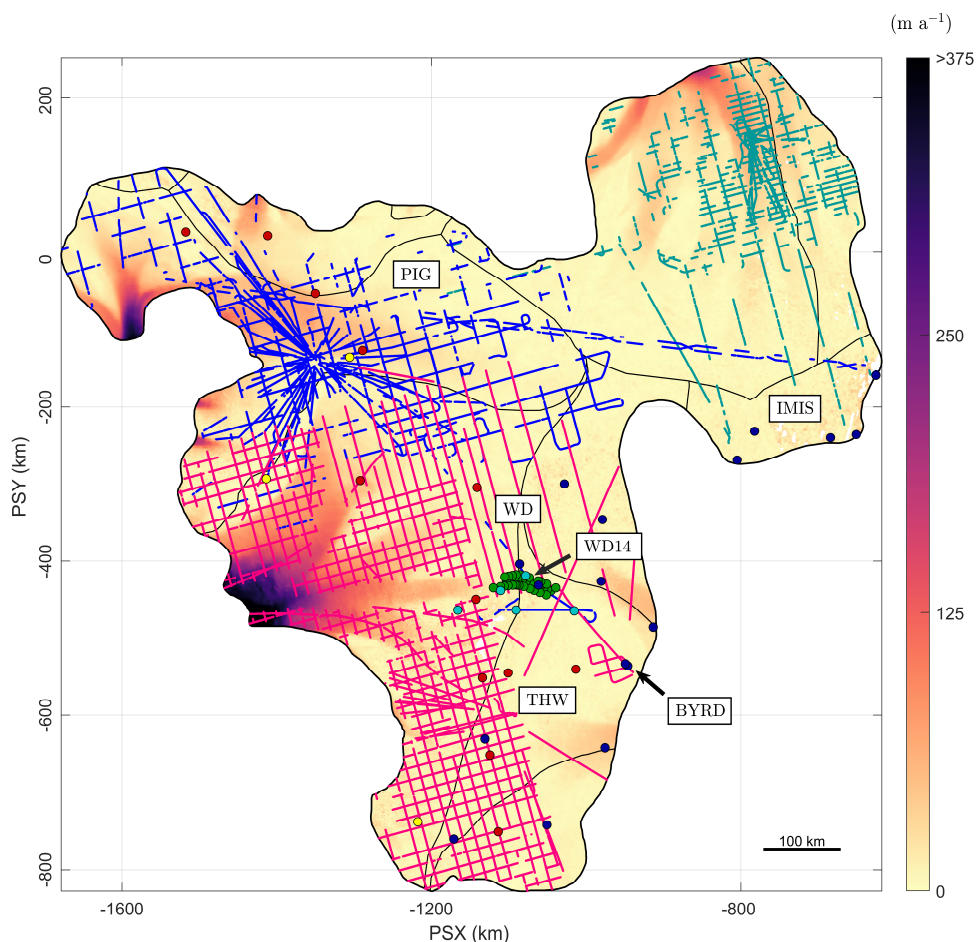
104 Here, our aim is to estimate mid-Holocene accumulation rates across the WAIS from first-
105 order calculations using a local-layer approximation (LLA) model (Waddington et al., 2007),
106 informed by the spatially extensive 4.72 ka IRH. We first describe the data and the 1-D model, and
107 discuss the methods used to assess the feasibility of the LLA from gradients in horizontal ice-flow, ice
108 thickness and accumulation-rate. We then present our accumulation rate estimates and discuss the
109 effects of spatial and topographic controls on our results in relation to modern accumulation rates
110 using both modelled gridded data from the Regional Atmospheric Climate Model 2 (hereafter
111 RACMO2; Van Wessem et al., 2018) and observational point-based data from snow, firn and ice
112 cores (Neumann et al., 2008; Burgener et al., 2013; Favier et al., 2013; Mayewski and Dixon, 2013;
113 Medley et al., 2014), to generate a long-term perspective on changes between the mid-Holocene and
114 the present. Finally, we place our results in the context of previous studies that consider the evolution
115 of the WAIS during the Holocene.

116 **2. Datasets and methods**

117

118 **2.1 Along-track IRH data**

119 We used data from extensive (~91 000 flight-track km) RES surveys acquired across West
120 Antarctica between 2004 and 2018. The main contributing surveys are the University of Texas
121 Institute for Geophysics (UTIG) 2004-2005 AGASEA survey flown over Thwaites Glacier (THW)
122 and Marie Byrd Land which deployed the 60-MHz High Capability Airborne Radar Sounder
123 (HiCARS) radar system (Holt et al., 2006; Peters et al., 2007), and the British Antarctic Survey (BAS)
124 2004-05 BBAS survey over Pine Island Glacier (PIG) and 2010-2011 IMAFI survey over Institute
125 and Möller Ice Streams (IMIS) which deployed the 150-MHz Polarimetric Airborne Survey
126 INstrument (PASIN) radar system (Vaughan et al., 2006; Corr et al., 2007; Ross et al., 2012; Fremand,
127 Bodart et al., 2022) (Fig. 1; Table 1). Additional profiles from NASA's Operation Ice Bridge (OIB;
128 MacGregor et al., 2021) 2016 and 2018 surveys, flown with the 190-MHz Multichannel Coherent
129 Radar Depth Sounder 2 (MCoRDS-2) radar system (CReSIS, 2018), were also used to extract IRH
130 information near the WD14 Ice Core and upper IMIS catchments (Bodart et al., 2021a; Figure 1 and
131 Table 1). We refer the reader to the above references for comprehensive details on each system's
132 capabilities.



133

134 Figure 1. Map of the datasets and key locations in this study. The three datasets that contain the 4.72 ka
135 IRH are color-coded as IMIS (green), PIG (blue), and THW (pink). IRHs falling outside $D > 1$ (see Section
136 2.2.1; Figure S1) are excluded. Points on the map represent the snow, firn and ice cores used in this study to
137 compare modern rates of accumulation with our 4.72 ka-to-present estimates (see Section 2.4 for source
138 references). The background colour map shows modern surface speeds from Rignot et al. (2017). Locations
139 mentioned in this paper are abbreviated on the map, as follows: BYRD (Byrd Ice Core), IMIS (Institute and
140 Möller Ice Streams), PIG (Pine Island Glacier), THW (Thwaites Glacier), WAIS (West Antarctic Ice Sheet),
141 WD (Western Divide), WD14 (WAIS Divide Ice Core). Major ice divides are from Mougnot et al. (2017).
142 Projection for all figures in this paper is WGS84 Antarctic Polar Stereographic (PSX/PSY; EPSG: 3031).

143 These RES surveys were used to track and date six IRHs spanning much of the Holocene and
144 Late Pleistocene across IMIS (Ashmore et al., 2020a), PIG (Bodart et al., 2021a) and THW (Muldoon
145 et al., 2018), collectively spanning much of the WAIS. Here we only consider the 4.72 ka IRH
146 mapped in all three studies and shown in Figure 1, as it is by far both the most spatially extensive and
147 the only commonly traced IRH across all studies. We first merged all data points from the 4.72 ka
148 IRH across the three catchments, resulting in a cumulative distance of ~40 000 line-km of IRH
149 profiles (44% of the RES surveys' total coverage; Table 1). Although the along-track RES data were
150 acquired with a trace spacing of between 10 and 35 m, depending on the dataset used, we re-sampled
151 these points to 500 m in the along-track direction. We then added a spatially invariant firn correction



152 of 10 m onto the Muldoon et al. (2018) dataset to match the same firn correction applied by the other
 153 studies to correct the IRH depth, and finally calculated the median value of all ice thicknesses and
 154 IRH depths falling within the nearest 500 m interval.

155 Table 1. Characteristics of each IRH dataset used in this study that contain the 4.72 ka IRH. ‘Reflector
 156 1’ in Muldoon et al. (2018) is abbreviated here as ‘R1’.

<i>Survey name</i>	<i>Survey provider</i>	<i>RES system</i>	<i>Dataset reference</i>	<i>Cumulative IRH distance (km)</i>
IMAFI	BAS	PASIN 150-MHz	H2 in Ashmore et al. (2020a)	1.5x10 ⁴
BBAS / OIB	BAS / NASA	PASIN 150-MHz / MCoRDS-2 190-MHz	R2 in Bodart et al. (2021a)	0.6x10 ⁴
AGASEA	UTIG	HiCARS 60-MHz	R1 in Muldoon et al. (2018)	1.9 x10 ⁴

157 2.2 Inferring accumulation rates

158 To infer accumulation rates from the 4.72 ka IRH, we used the Nye model, a 1-D ice-flow
 159 model widely used for estimating accumulation rates and age-depth relationships over relatively slow-
 160 flowing parts of an ice sheet (Nye, 1957; Fahnestock et al., 2001). Other 1-D models exist, including
 161 the Dansgaard-Johnsen (Dansgaard and Johnsen, 1969) and the shallow-strain rate model (MacGregor
 162 et al., 2016), but neither were suitable for this study due to uncertainties in the basal shear layer
 163 thickness across our survey area and because we are limited to only one IRH to constrain the ice-flow
 164 model. The Nye model assumes that ice thickness is constant and therefore that the ice sheet has been
 165 in a steady state since the deposition of the IRH, a realistic assumption for the period under
 166 investigation here. The Nye model states:

$$167 \dot{b}_a = \ln\left(\frac{z_a}{H} \frac{H}{a}\right), \quad (1)$$

168 where \dot{b}_a is the mean surface-accumulation rate during the Holocene epoch between an IRH of age a
 169 and the present, z_a represents the depth of the IRH dated at the ice core, and H is the ice thickness.
 170 The model assumes that the vertical strain rate, $\dot{\epsilon}_a$, is also constant and vertically uniform, so that it
 171 exactly balances the overburden of local ice accumulation:
 172
 173

$$\dot{\epsilon}_a = \frac{\dot{b}_a}{H}. \quad (2)$$

174 We iterated Eq. (1) over the re-sampled 500-m spaced dataset using the depth of the 4.72 ka
 175 IRH for z_a and used the median radar-derived ice-thickness measurement re-sampled over the 500-m
 176 grid to obtain H , when this information was available. In areas where the radar did not sound the bed,
 177 we used the BedMachine v2 gridded product to obtain a value for H (Morlighem, 2020). Note that the
 178 accumulation values presented in this study are all reported in m a⁻¹ of ice equivalent.

179 Uncertainties in accumulation rates are calculated by iterating Eq. (1) using the lowest and
 180 highest possible age of the 4.72 IRH based on the maximum and minimum age uncertainty (± 0.28 ka)
 181 calculated from RES and ice-core depth uncertainties (see details in Muldoon et al. (2018) and Bodart
 182 et al. (2021a)). This results in lower and upper bounds in accumulation rates over our model domain
 183 (Fig. S2a-b), which are then combined to provide a relative uncertainty in accumulation rates for the
 184 4.72 ka IRH (Fig. S2c). The maximum relative uncertainty in accumulation rates for the 4.72 ka IRH
 185 is 3.3%, with a median value of <0.5% across our grid. Note that these values do not include



186 uncertainties due to the model approximation itself. As discussed in the next two sections, we believe
187 model uncertainties to be small for the domain considered.

188 **2.2.1 Assessing the suitability of the 1-D model**

189 To quantify the suitability of the LLA onto which the 1-D model is based, we calculated the
190 effects of horizontal gradients in modern ice thickness and accumulation rates along particle paths in
191 their ability to affect IRH depths, as per Waddington et al. (2007). In places where these gradients are
192 too large, estimates of accumulation rates from IRHs likely require a more complete treatment of ice
193 flow and strain rates to account for disturbances in IRH depths, which only multi-dimensional models
194 are able to resolve (Waddington et al., 2007; Koutnik et al., 2016; MacGregor et al., 2016).

195 To quantify the effect of horizontal gradients on IRH of age a , we computed the total
196 horizontal particle path length L_{path} and characteristic lengths L_H and L_b representing the gradients in
197 ice thickness and accumulation rates respectively for age a (Supplementary Information). These three
198 components were then combined to generate a non-dimensional parameter D (Fig. S1d). Waddington
199 et al. (2007) and MacGregor et al. (2009; 2016) used a maximum D value of unity to estimate where
200 the LLA is acceptable, but because the value of D cannot yet be translated quantitatively into an
201 uncertainty value for an LLA-inferred accumulation rate, it is not clear what value is appropriate.
202 Smaller values of D indicate that local horizontal gradients in ice thickness and accumulation rates
203 have a smaller effect on IRH depth of age a , and thus we assume that the LLA is valid (Waddington
204 et al., 2007; MacGregor et al., 2009; 2016). However, if $D > 1$, we assume that the depth of the IRH is
205 unlikely to be the sole result of accumulation rates at the surface and that a more sophisticated model
206 is required (Sect. 2.2.2). In our case, most of the survey areas has D values that are well below the
207 unity, except for a limited number of IRH profiles near the onset of PIG's tributaries and over THW's
208 central trunk, which we excluded from our analysis.

209 **2.2.2 Model limitations**

210 One of the limitations of the Nye model is that it assumes that gradients in sliding velocity are
211 mostly concentrated in a thin layer at the ice-bed interface and that the ice column deforms by pure
212 shear only (Nye, 1957; Fahnestock et al., 2001). For this reason, the Nye model is generally only
213 appropriate for IRHs found in the upper part of the ice column, as is the case here. Additionally, the
214 use of the model is restricted to areas where ice flow is slow and horizontal strain rates are low.

215 Multi-dimensional models would likely improve the accumulation estimates for IRHs found
216 in the lower half of the ice column or in more disrupted or faster flowing areas (e.g. Waddington et
217 al., 2007; Neumann et al., 2008; MacGregor et al., 2009; Leysinger Vieli et al., 2011; Karlsson et al.,
218 2014; Koutnik et al., 2016; Sutter et al, 2021). However, we focus on a shallower IRH situated within
219 the upper 40% of the ice column (Fig. 2b-c), where we can be reasonably confident that the ice sheet
220 has remained close to steady-state and where IRHs are likely shallow enough not to have sustained
221 appreciable disturbances that would affect the Nye model assumptions (Sect. 2.2).

222 Additionally, due to the inherent nature of tracking IRHs through RES data, our coverage is
223 limited to areas where ice-flow speeds are low and IRHs are relatively undisturbed. An assessment of
224 strain rates over our model domain suggests limited disturbance over the WD and most of our grid,
225 apart from near the onset of faster flow at the boundaries of our grid with the trunks of PIG and THW
226 where higher strain rates are observed (Fig. S3). This pattern, combined with the assessment of the
227 suitability of the LLA (Sect. 2.2.1) and exclusion of IRHs outside of the $D > 1$ boundary, supports our
228 application of a 1-D modelling approach here.

229 **2.3 Gridding and filtering**



230 Once IRH depths and accumulation rates for the 4.72 ka IRH were obtained at regular 500-m
231 points along RES flight paths, we filtered the results using a moving-average Gaussian filter of length
232 30 samples (equivalent to ~15 km) to reduce along-track noise in the IRH depth, and then gridded the
233 filtered result using a Delaunay-triangulation-based natural neighbour interpolation method onto a 1-
234 km polar stereographic grid. We further smoothed the gridded data using an 18-km square cell mean
235 filter to limit the localised artefacts arising from the interpolation, which can be problematic in areas
236 with poor data coverage. Figure S4 shows the maximum distance away from the nearest 500-m along-
237 track point used to produce Figures 2-3, and thus where errors in the interpolated grids are expected to
238 be larger. The median value of this maximum distance is 5 km and its maximum value is 75 km,
239 which is comparable to previous studies (e.g. Medley et al., 2014). We evaluated other possible
240 interpolation methods (e.g., kriging and using different semi-variogram models), but they resulted in
241 similar or poorer quality, and were thus discounted.

242 **2.4 Comparison with modern observations**

243 To compare our inferred accumulation estimates for the past 4.72 ka with modern times
244 (defined here as 1651-2019), we derived information on modern accumulation rates from two sources,
245 one modelled (gridded) and one from a series of observational (point-based) datasets.

246 We used modelled gridded accumulation rates from the RACMO 2.3p2 1979-2019 Surface
247 Mass Balance (SMB) product forced at its margin with the ERA-Interim product (native resolution:
248 27 km) as an estimate for modern accumulation rates (Van Wessem et al., 2018). Although SMB is
249 not technically equivalent to the accumulation rate, runoff and sublimation are negligible in our
250 survey area (Medley et al., 2013) so we consider SMB equal to accumulation rate in this region. We
251 converted modelled values from $\text{kg m}^{-2} \text{a}^{-1}$ to m a^{-1} of ice equivalent using an ice density value of 917
252 kg m^{-3} , calculated the 40-year mean, and then bi-linearly interpolated the gridded RACMO2 product
253 to the same 1-km grid resolution as our 4.72 ka-to-present accumulation grid (Sect. 2.3) to ensure
254 consistency when comparing both datasets.

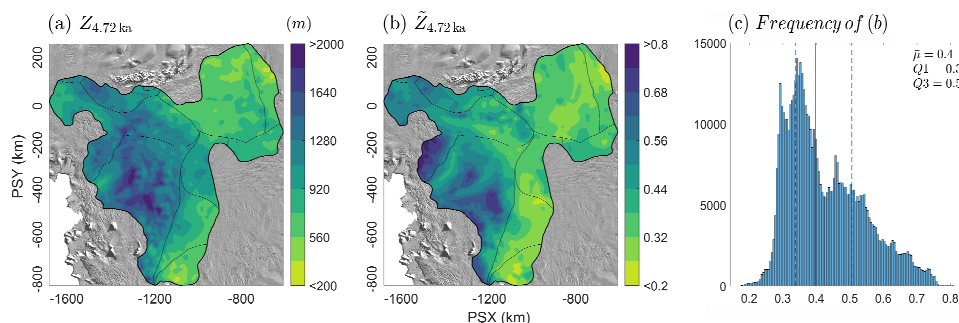
255 Observational point-based measurements were obtained from a series of snow, firn and ice
256 cores from the ITASE (Mayewski and Dixon, 2013), MED14 (Medley et al., 2014), SAMBA (Favier
257 et al., 2013), and SEAT-10 (Burgener et al., 2013) datasets, as well as from a network of centennially-
258 averaged modern accumulation rates derived from shallow IRHs traced on ground-based RES data
259 over the WD and dated using a shallow ITASE Ice Core (Neumann et al., 2008) (Fig. 1). This results
260 in 79 point-based accumulation measurements covering the period 1651-2010 CE (Common Era) and
261 spread across our model domain (see Figure 1). Further detail on these datasets can be found in the
262 above references. To compare the Holocene gridded product with the point-based measurements, we
263 first calculated the average value of the accumulation rate at the point measurement for the entire
264 period. We converted this value to ice-equivalent accumulation rates (as above) and extracted the two
265 paired values, i.e., the value for the point-measurement for modern accumulation rates and the value
266 for the nearest grid cell in the gridded 4.72 ka-to-present accumulation estimates to this measurement.

267 **3. Results**

268 The final grids for depth and accumulation rates for the 4.72 ka IRH are shown in Figures 2-3. In
269 total, these grids are made of ~89 000, 500-m spaced points, which cover an area of ~610 000 km^2 , or
270 ~30% of the total surface area of the WAIS. The grids span most of PIG and THW glacier
271 catchments, as well as the Ronne (upper Rutford, Institute, and Möller) and upper western Ross
272 (Bindschadler, Kamb, MacAyeal, and Whillans) catchments (IPY Antarctic boundaries G-H, J-Jpp,
273 and Ep-F; Mouginot et al. (2017); Fig. 1-2). Overall, the 4.72 ka IRH is shallower within the IMIS
274 and upper PIG and THW catchments, as well as on the Ross side of the WD where ice thickness is
275 particularly deep (Fig. 2b). Conversely, the 4.72 ka IRH is deeper in the ice near a 400-m high
276 bedrock plateau that separates the northern and southern basins of PIG (Vaughan et al., 2006) and at



277 two locations in the upstream parts of the main trunk of THW where ice flows over highs in
 278 subglacial topography (Fig. 2b).

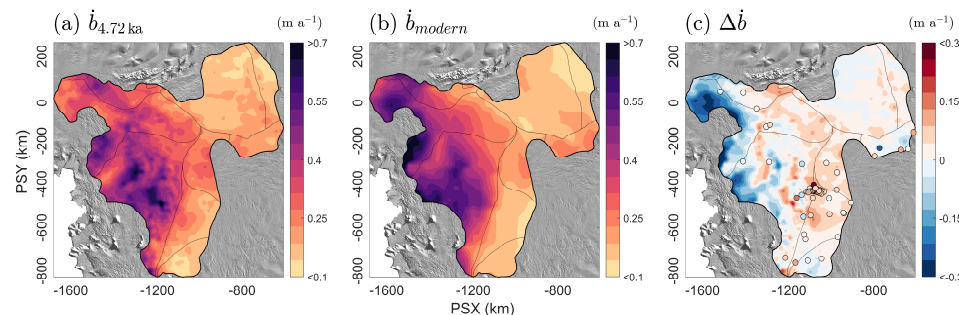


279

280 Figure 2. Gridded depths for the 4.72 ka IRH across the model domain covering the PIG, THW, and
 281 Institute and Möller ice-stream catchments. (a) Gridded depth of the 4.72 ka IRH. (b) Normalised depth of the
 282 4.72 ka IRH relative to ice thickness. (c) Histogram showing the distribution of values in (b) with the median
 283 ($\bar{\mu}$) and the interquartile range (i.e. 25th (Q1) and 75th (Q3) quartiles) shown as solid and dashed blue lines
 284 respectively. The background image is the 2014 MODIS mosaic of Antarctica (Haran et al., 2018).

285 3.1. Catchment-scale accumulation estimates

286 Figure 3 shows a comparison of the ice-equivalent accumulation rates we inferred for the 4.72
 287 ka IRH (Fig. 3a) and modern SMB estimates from RACMO2 (Fig. 3b). We observe that the IRH
 288 accumulation rate pattern for the last 4.72 ka is similar to the modern pattern of accumulation rates for
 289 the Amundsen Sea sector of the WAIS, which is dominated by higher coastal accumulation rates that
 290 progressively decrease inland towards the ice divides (Fig. 3a-b). Differences in accumulation
 291 between the 4.72 ka-to-present estimates and modern values are mainly observed directly upstream of
 292 the main trunks of PIG and THW, where modern rates are much higher (up to 0.2 m a^{-1} ice
 293 equivalent) than for the 4.72 ka-to-present estimates (Fig. 3c). In comparison, higher accumulation
 294 rates for the last 4.72 ka compared to modern rates are observed for the entire stretch of the WD (Fig.
 295 3c; Table 2). Noticeably over the IMIS catchment, little change is observed between the two periods.
 296 Over the entire model domain, we observe a median relative increase of 13% in accumulation rates
 297 since 4.72 ka compared with modern rates (Fig. 4; Table 2); however, when considering only the
 298 values that fall within 100 km of either side of the WD (where mean surface speeds equal $\sim 7 \text{ m a}^{-1}$),
 299 we obtain a median value of 18% higher accumulation compared with modern accumulation rates
 300 (Fig. 4).



301

302 Figure 3. Gridded estimates of ice-equivalent accumulation rates for the last 4.72 ka and modern times.
 303 (a) Gridded accumulation rates inferred from the 4.72 ka IRH. (b) Modern (1979 – 2019) modelled SMB rates
 304 from RACMO2. (c) Difference between 4.72 ka-to-present and modern accumulation rates (red = 4.72 ka-to-



305 present accumulation higher than modern times, blue = 4.72 ka-to-present accumulation lower than modern
306 times). The dots represent the difference between the value for the nearest grid cell in (a) and averaged
307 accumulation rates at 79 core locations (see Section 2.4). The background image is the 2014 MODIS mosaic of
308 Antarctica (Haran et al., 2018).

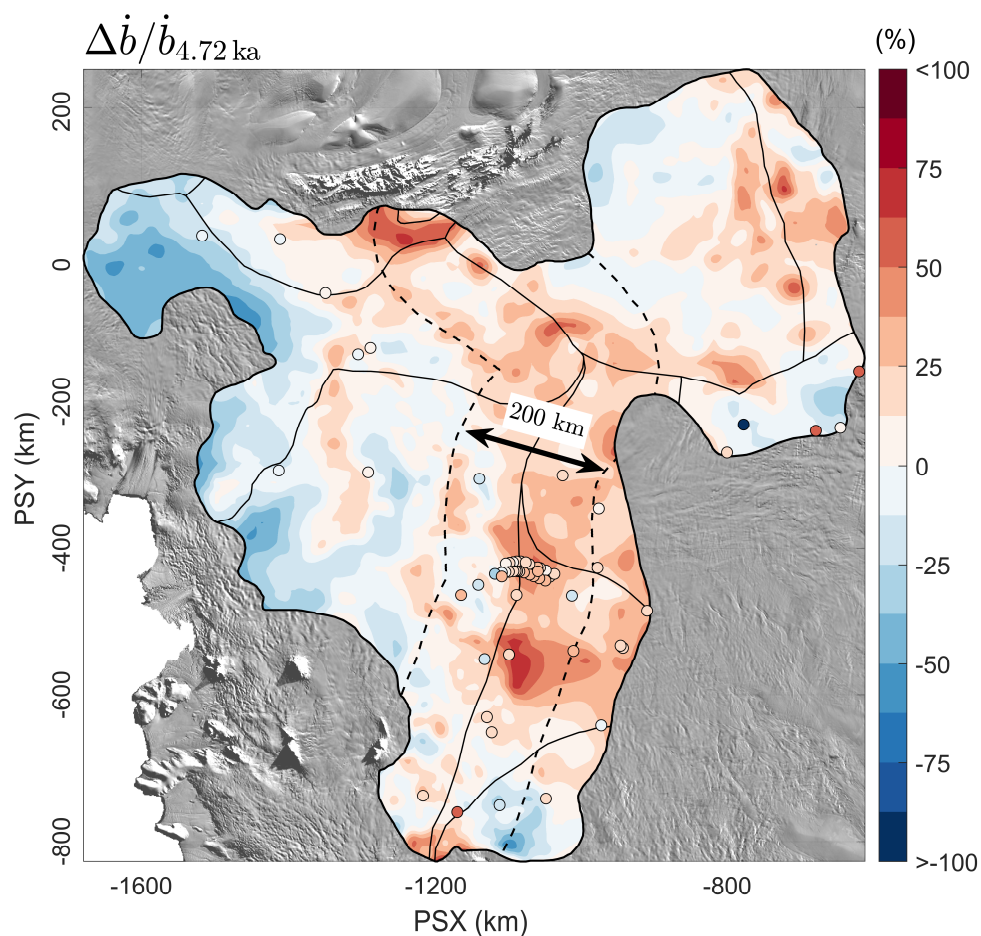
309 Comparison between our 4.72 ka-to-present accumulation-rate estimates and 79 point-based
310 accumulation measurements for modern times (1651-2010 CE) are shown in Figure 3 and 4. This
311 evaluation shows that the 4.72 ka-to-present accumulation-rate estimates for the nearest grid cell to
312 each point measurement are, on average, 18% ($p < 0.0015$, $n=79$) higher over the entire grid and 19%
313 ($p < 0.0001$, $n=59$) higher within 100 km of the divide than modern accumulation rates (Fig. 4). This
314 result confirms that the relative difference in gridded accumulation rates between the 4.72 ka-to-
315 present and modern modelled accumulation rates is consistent with modern rates from point-based
316 measurements.

317 Table 2. Summary statistics for the modern (modelled and observational) and 4.72 ka-to-present ice-
318 equivalent accumulation rates at the catchment-scale and over the WD. Values for the WD are for all points that
319 fall within 100 km of either side of the divide (see dashed line in Figure 4). $\bar{\mu}$ refers to the median and IQR
320 represents the Interquartile Range calculated by computing the difference between the 75th and 25th percentiles.

Accumulation rate ($m a^{-1}$)	Catchment-wide		WD only	
	$\bar{\mu}$	IQR	$\bar{\mu}$	IQR
Modern (model)	0.23	0.23	0.22	0.10
Modern (cores)	0.24	0.12	0.24	0.09
4.72 ka-to-present	0.27	0.18	0.27	0.11

321

322 For WD14 specifically, the nearest grid node to the ice-core site shows a 22% higher
323 accumulation rate from 4.72 ka to present compared with modern accumulation rates (Fig. 4). There,
324 our IRH-inferred accumulation rate is $0.28 \pm 0.01 m a^{-1}$, with the nearest IRH point situated 1.2 km
325 away from WD14 showing an accumulation rate of $0.27 \pm 0.01 m a^{-1}$. This is only slightly higher than
326 the direct ice-core reconstruction of accumulation rates at WD14, which show up to 19% ($0.25 m a^{-1}$)
327 higher accumulation than modern rates ($0.21 m a^{-1}$) since 4700 years BP (Fudge et al., 2017).



328

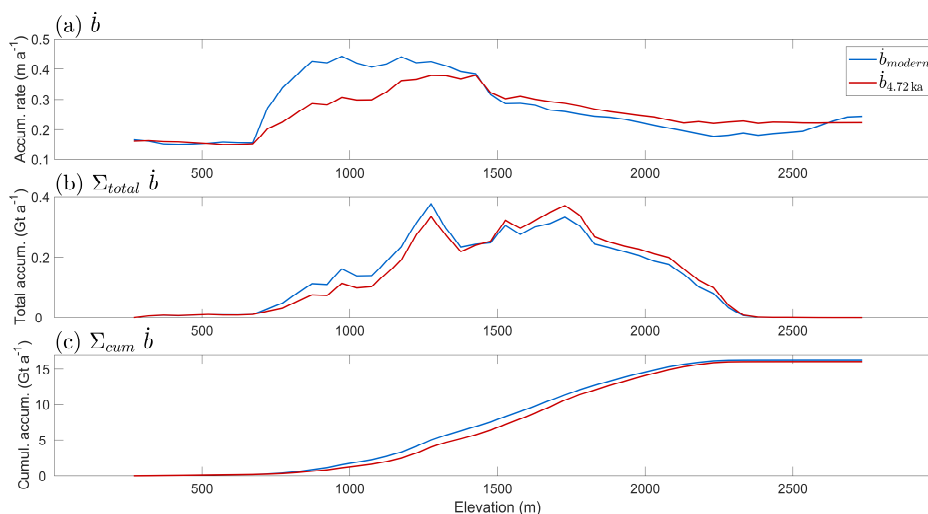
329 Figure 4. Relative difference in accumulation rates between the 4.72 ka-to-present estimates and
330 modern rates. The points on the map represent the relative difference in ice-equivalent accumulation rate
331 between the nearest grid cell in the 4.72 ka-to-present grid and the 79 observational accumulation measurements
332 from snow, firn, and ice cores (Fig. 1; see Sect. 2.4). The dashed outline line represents the 100-km boundary on
333 either side of the WD used to provide the summary statistics in Section 3.1 and Table 2. The background image
334 is the 2014 MODIS mosaic of Antarctica (Haran et al., 2018).

335 3.2 Elevation-dependent accumulation estimates

336 While Figures 3 and 4 help to assess potential differences in patterns and rates across spatial
337 scales, considering accumulation-rate differences in terms of elevation can inform how topography
338 influences accumulation and whether this has changed over time. As a result, we binned the ice-
339 equivalent accumulation values for each 50-m elevation bands across our model domain for both the
340 4.72 ka-to-present estimates and modern (RACMO2), and calculated the mean accumulation rate, the
341 total accumulation rate, and the cumulative sum of total accumulation rate for each bin over the entire
342 elevation gradient of the two grids (Fig. 5). As above, we observe that the accumulation-rate estimates
343 for the period since 4.72 ka are lower at lower elevations (~700 – 1400 m) compared with RACMO2,
344 and overtake RACMO2 near the 1400-m elevation band where 4.72 ka-to-present accumulation is
345 higher than modern times across the divide up until ~2600 m in elevation (Fig. 5a). The lack of a large
346 difference between the two datasets at elevations of ~250 – 700 m is primarily dominated by



347 accumulation rates over IMIS, which, in contrast to the PIG and THW regions, is less exposed to the
348 large accumulation gradients characteristic of the Amundsen Sea Embayment, i.e. higher coastal
349 accumulation decreasing inland.



350

351 Figure 5. Comparison of ice-equivalent accumulation rates between the 4.72 ka-to-present estimates
352 and modern rates (RACMO2) binned for each 50-m elevation bands across our study. (a) Mean accumulation
353 rate averaged per 50-m elevation band across the survey area in m a^{-1} . (b) Total accumulation rate per 50-m
354 elevation band in Gigatons per annum (Gt a^{-1}). (c) Cumulative sum of total accumulation rate per 50-m
355 elevation band in Gt a^{-1} .

356

4. Discussion

357 Previous studies of past accumulation rates over the WAIS have shown that accumulation varied
358 temporally during the Holocene. Using a single airborne RES profile over the Amundsen Sea sector,
359 Siebert and Payne (2004) showed that accumulation rates were approximately the same at 3.1 ka
360 compared with modern rates, but $\sim 0.3 \text{ m a}^{-1}$ greater ($\sim 15\%$) than current rates between 3.1-6.4 ka,
361 before which accumulation was $\sim 50\%$ of modern rates between 6.4 and 16.0 ka. Similarly, Neumann
362 et al. (2008) found that accumulation rates at the WD were $\sim 30\%$ higher between 3-5 ka than modern
363 values based on a dense network of IRHs traced on ground-based RES data, while Karlsson et al.
364 (2014) found that accumulation patterns had likely changed twice during the early to mid-Holocene
365 over PIG from the lack of a model fit between the depths and ages of two prominent IRHs. Using the
366 updated WD14 record, Fudge et al. (2016) showed that accumulation was higher there in the mid to
367 late-Holocene (19% between 4.72 ka BP and the present), a trend that was also observed by Koutnik
368 et al. (2016), who found a 20% increase in accumulation rates between 2-4 ka compared with modern
369 rates from a ground-based RES profile across the ice divide. In showing that mean accumulation rates
370 since 4.72 ka were 18% greater than modern rates across the WD, our results provide a much wider
371 regional picture (across $\sim 30\%$ of the WAIS) that accumulation during the mid-Holocene exceeded
372 modern rates over large parts of West Antarctica.

373 We gain confidence in the ability of the Nye model to estimate past accumulation rates from the
374 4.72 ka IRH, given that its outputs match relatively well with the direct reconstruction of mean
375 accumulation rates at the WD14 Ice Core, with values at the ice core of $0.27 \pm 0.01 \text{ m a}^{-1}$ (this study)
376 compared with 0.25 m a^{-1} for Fudge et al. (2016). This also suggests that the WD14 Ice Core suitably
377 represents atmospheric conditions across the wider WD. A possible explanation for the higher
378 accumulation rates during the mid-Holocene compared with modern values is that they represent a



379 continued climatic transition from the LGM (Steig et al., 2001). Alternatively, it has been suggested
380 that seasonal or interannual variability, such as a weaker circumpolar vortex (Van Den Broeke and
381 Van Lipzig, 2004; Neumann et al., 2008) or teleconnections to tropical Pacific Ocean warming
382 (Sproson et al., 2022), may also lead to such difference. We did not find evidence for significant
383 changes in accumulation patterns between the mid-Holocene and modern times, suggesting that the
384 current spatial pattern of high accumulation at the coast, decreasing inland towards the divide has
385 been stable throughout the mid-Holocene over PIG and THW, as previously suggested by others
386 (Siegert and Payne, 2004; Neumann et al., 2008).

387 Accumulation estimates for the 4.72 ka-to-present are smaller than modern rates in the lowest
388 elevation bands (i.e. <1400 m) (Figs. 4, 5). This pattern was also reported by Medley et al. (2014),
389 who compared modern observational and modelled data within the ASE and hypothesised that this
390 discrepancy at low elevations resulted primarily from a lack of sufficient accumulation measurements
391 in the lower sections of their survey area. In our case, these low-elevation values are close to the
392 boundary where we consider the LLA acceptable for the 4.72 ka IRH, albeit where D values are
393 higher than for the rest of the catchment (Figure S1d), so it is more likely that accumulation rates
394 calculated there are affected by ice-flow gradients and their influence upon IRH depths. Despite this
395 caveat, Figure 5b shows that values at low elevations (250 – 1200 m) contribute relatively little to the
396 total accumulation (by mass) over our survey area.

397 Our results reinforce the evidence that accumulation rates have varied temporally across West
398 Antarctica during the Holocene, a finding that must be considered by future modelling studies that
399 simulate past sea-level rise from Antarctica since the LGM. Model results from Steig et al. (2001)
400 suggest that the maximum elevation of the WAIS was most likely reached during the early to mid-
401 Holocene (around ~7 ka) following higher accumulation rates at the late glacial–interglacial
402 transition, after which elevations slowly declined to present conditions as the sea-level-rise-induced
403 kinematic wave reached the ice-sheet interior and outpaced the increase in accumulation rates.
404 However, a moderate mid-Holocene increase in accumulation rates, which our results suggest
405 occurred widely across the WAIS, would, if sustained, likely delay the timing of the decline in
406 elevation by several thousand years (Steig et al., 2011). Using a flowband model, Koutnik et al.
407 (2016) suggested that the increase of up to 40% in accumulation rates for the period 9 – 2 ka would
408 likely lead to an increase in ice thickness of tens of meters during the mid-Holocene. However,
409 because the WAIS is also sensitive to ice-dynamical changes at the ice-sheet margins (e.g. GL retreat
410 and/or calving), an increase in accumulation rates in the upper part of the ice sheet may not
411 necessarily result in enough thickening to counteract potential losses from ice dynamics further
412 downstream (Jones et al., 2022). The lack of an ice-dynamical component in the model used here
413 precludes us from reaching such a conclusion; however, higher accumulation rates of up to 18%
414 during the mid-Holocene across 30% of the WAIS would likely be consistent with an increase of
415 several tens of meters in ice thickness (e.g. Figure 10 of Koutnik et al., 2016). This potential increase
416 in surface elevation is unlikely to affect the steady-state assumption of the 1-D model used here,
417 considering that these changes are small (a few per cent of the ice thickness) and that ice thickness
418 exceeds 3500 m in places over our survey area. We encourage future ice-sheet models to test a range
419 of scenarios that would account for variable accumulation rates between the LGM and the present
420 over the WAIS by using the WD14 reconstructed accumulation rates from Fudge et al. (2016) as a
421 guide, which, as we show here, suitably represents the pattern of accumulation variability over both
422 time and space in West Antarctica.

423 We may also consider the possibility for Holocene ice thickening at the divide from increased
424 accumulation to affect GL evolution over the WAIS. Recent evidence from ice-sheet modelling and
425 field measurements suggests that GL retreat during the Holocene was not monotonic, particularly at
426 the Ross and Weddell Sea sides of the WAIS (Bradley et al., 2015; Kingslake et al., 2018; Neuhaus et
427 al., 2021). Rather, Kingslake et al. (2018) showed that the GL position in the Ross and Weddell Sea



428 sectors initially retreated from the LGM inland until $\sim 9.7 - 10.2$ ka, and then re-advanced to its
429 modern position sometime during the Holocene. Although they attributed this change in GL position
430 to the solid Earth viscoelastic response due to ice-sheet mass change and the subsequent re-grounding
431 around pinning points, it has also been suggested that an increase in accumulation rates upstream of
432 the GL could lead to a re-advance via ice thickening there and a subsequent increase in ice flow (Steig
433 et al., 2001; Koutnik et al., 2016; Jones et al., 2022).

434 Across parts of the Weddell Sea Embayment, several studies (Ross et al., 2011; Hein et al., 2016;
435 Ashmore et al., 2020a) have produced evidence for stability of the LGM ice thickness there until the
436 early to mid-Holocene, contrary to most of the WAIS, after which abrupt thinning of ~ 400 m
437 contributed $\sim 1.4 - 2$ m of sea level rise (Hein et al., 2016). A possible explanation for this delayed
438 thinning in the Weddell Sea Embayment is that increased snowfall in the upper WAIS might have
439 counteracted ice-dynamical processes at the coast until the mid to late Holocene (Hein et al., 2016;
440 Spector et al., 2019). Similarly, over part of the Ross Sea sector, Neuhaus et al. (2021) showed that
441 the GL over Whillans, Kamb, and Bindschadler ice streams retreated to its minimum Holocene
442 position in the mid to late-Holocene, and then re-advanced between $1 - 2$ ka, coinciding with periods
443 of warmer and colder climates, respectively. They concluded that the reported GL migration was
444 likely dominated by modest climate-induced changes upstream rather than ice dynamics further
445 downstream, as suggested for the Weddell Sea sector (Hein et al., 2016). Our results, which provide
446 strong and widespread evidence for higher accumulation rates at the WD during the mid-Holocene,
447 supports further this hypothesis, as more accumulation at the divide would likely result in upstream
448 thickening, which, in the absence of ice-dynamical processes counter-balancing this increase in
449 accumulation, would result in GL advance in the Ross and Weddell Sea regions. We note that the
450 increase in accumulation at $\sim 4 - 5$ ka represents the peak of a period of higher accumulation initiated
451 from ~ 7 ka onwards at the WD14 Ice Core (Fudge et al., 2016), thus it is likely that our accumulation
452 estimates form part of a wider pattern of sustained accumulation across the WD over several
453 millennia. This noted, the pattern of GL retreat and re-advance has not been observed over the
454 Amundsen Sea sector (Kingslake et al., 2018; Johnson et al., 2020; 2021; Braddock et al., 2022)
455 despite the accumulation increase we observed along the WD, potentially indicating that this sector is
456 more controlled by changes in ice dynamics for which even moderate changes in accumulation rate
457 cannot compensate.

458 5. Conclusion

459 Using a ubiquitous Internal Reflecting Horizon found across most of the Pine Island, Thwaites,
460 and Institute and Möller ice-stream catchments, we have estimated mid-Holocene accumulation rates
461 in the slow-flowing parts of West Antarctica (representing 30% of total surface area of the WAIS)
462 using a 1-D ice-flow model. By comparing our Holocene accumulation estimates with modern climate
463 reanalysis models and observational syntheses, we estimated that accumulation rates across the
464 Amundsen-Weddell-Ross Sea divide since 4.72 ka were, on average, 18% higher than modern
465 accumulation rates. While the accumulation rates have therefore varied temporally, our results suggest
466 that spatial patterns of accumulation between regions across the WAIS have remained similar during
467 this period, i.e., higher accumulation rates at the coast and lower accumulation rates at the ice divides.
468 The higher accumulation estimates reported here for the mid-Holocene agree well with previous,
469 more spatially-focused studies of accumulation rates across the WAIS, which all indicate higher
470 accumulation rates of between 15 and 30% over the last ~ 5 ka. Finally, our results further support the
471 use of the WAIS Divide ice-core record to assess past atmospheric conditions across the wider
472 Western Divide and even a substantial portion of the WAIS, making it a powerful dataset for ice-sheet
473 models. The higher accumulation rates reported here occurred at a time of asynchronous grounding-
474 line migration over the WAIS, including re-advances of the grounding-line in the Weddell and Ross
475 sectors and evidence for delayed deglaciation in the Weddell Sea side of the WAIS. We suggest that



476 ice-sheet models account for the evolution of accumulation rates over time when predicting past and
477 future sea level coming from West Antarctica instead of using a fixed Last Glacial Maximum value.

478 **Code availability**

479 All the codes used to produce the results presented in this paper will be made available on the
480 GitHub page of Julien A. Bodart (<https://github.com/julbod>, last accessed: 15 October 2022) and on
481 Zenodo (Bodart, 2023a) upon acceptance of this manuscript.

482 **Data availability**

483 The IRH information for each of the three surveys used in this paper are archived in open-
484 access repositories (Ashmore et al., 2020b; Bodart et al., 2021b; UTIG R1 layer to be made available
485 via USAP-DC in due course) with references and links provided in the reference list. The BAS
486 airborne radar data which were used to extract the IRHs used in this paper are fully available at the
487 UK Polar Data Centre via the Polar Airborne Geophysics Data Portal (see Fremand, Bodart et al.,
488 2022). The full RACMO 2.3p2 product is available on request from j.m.vanwessem@uu.nl or
489 m.r.vandenbroeke@uu.nl. Links to access the observational point-based datasets used here are
490 available from the respective references mentioned in the text (Section 2.4). The gridded depth and
491 accumulation output from this study will be archived at the UK Polar Data Centre upon acceptance of
492 this manuscript (Bodart et al., 2023b).

493 **Author contribution**

494 J.A.B. designed the study with supervision from R.G.B., D.A.Y., and D.D.B. J.A.B.
495 performed the data processing, gridding, and 1-D modelling, with contributions from J.A.M. for the
496 modelling approach. J.A.B. interpreted the results with input from R.G.B., D.A.Y., D.D.B., and
497 J.A.M. J.A.B. wrote the paper, with edits from all co-authors.

498 **Competing interests**

499 The authors declare that they have no conflict of interest.

500 **Acknowledgments**

501 This study was motivated by the AntArchitecture SCAR Action Group. UTIG acknowledges
502 the high school students who did the original AGASEA layer interpretation.

503 **Financial support**

504 J.A.B. was supported by the NERC Doctoral Training Partnership grant (NE/L002558/1),
505 hosted in the Edinburgh E³ DTP program. J.A.B. also acknowledges the Scottish Alliance for
506 Geoscience, Environment and Society (SAGES) for funding a Postdoctoral and Early Career
507 Researcher Exchanges scheme to UTIG. Support for UTIG data analysis was received from NSF
508 grant nos CDI-0941678, PLR-1443690, and PLR-10437661, as well as the G. Unger Vetlesen
509 Foundation and the UTIG Gale White and Ewing/Worzel Fellowships. This is UTIG contribution
510 number: xxxx (TBD).

511 **References**

512 Arndt, J.E., Hillenbrand, C.D., Grobe, H., Kuhn, G. and Wacker, L.: Evidence for a dynamic
513 grounding line in outer Filchner Trough, Antarctica, until the early Holocene, *Geology*, 45(11), 1035-
514 1038, <https://doi.org/10.1130/G39398.1>, 2017.



- 515 Ashmore, D.W., Bingham, R.G., Ross, N., Siegert, M.J., Jordan, T.A. and Mair, D.W.:
516 Englacial architecture and age-depth constraints across the West Antarctic Ice Sheet, *Geophys. Res.*
517 *Let.*, 47 (6), p.e2019GL086663, <https://doi.org/10.1029/2019GL086663>, 2020a.
- 518 Ashmore, D.W., Bingham, R.G., Ross, N., Siegert, M., Jordan, T.A. and Mair, D.W.F.:
519 Radiostratigraphy of the Weddell Sea sector of West Antarctica, v2.0.0, Zenodo [data set],
520 <https://doi.org/10.5281/zenodo.4945301>, 2020b.
- 521 Beem, L.H., Young, D.A., Greenbaum, J.S., Blankenship, D.D., Cavitte, M.G., Guo, J. and
522 Bo, S.: Aerogeophysical characterization of Titan Dome, East Antarctica, and potential as an ice core
523 target, *The Cryosphere*, 15 (4), 1719-1730, <https://doi.org/10.5194/tc-15-1719-2021>, 2021.
- 524 Bingham, R.G. and Siegert, M.J.: Radio-echo sounding over polar ice masses. *J Environ. Eng.*
525 *Geoph.*, 12 (1), <https://doi.org/10.2113/JEEG12.1.47>, 47-62, 2007.
- 526 Bracegirdle, T.J., Colleoni, F., Abram, N.J., Bertler, N.A., Dixon, D.A., England, M., Favier,
527 V., Fogwill, C.J., Fyfe, J.C., Goodwin, I. and Goosse, H.: Back to the future: Using long-term
528 observational and palaeo-proxy reconstructions to improve model projections of Antarctic climate,
529 *Geosci. J.*, 9 (6), 255, <https://doi.org/10.3390/geosciences9060255>, 2019.
- 530 Braddock, S., Hall, B.L., Johnson, J.S., Balco, G., Spoth, M., Whitehouse, P.L., Campbell, S.,
531 Goehring, B.M., Rood, D.H. and Woodward, J.: Relative sea-level data preclude major late Holocene
532 ice-mass change in Pine Island Bay, *Nat. Geosci.*, 15, 568-572, [https://doi.org/10.1038/s41561-022-](https://doi.org/10.1038/s41561-022-00961-y)
533 [00961-y](https://doi.org/10.1038/s41561-022-00961-y), 2022.
- 534 Bradley, S.L., Hindmarsh, R.C., Whitehouse, P.L., Bentley, M.J. and King, M.A.: Low post-
535 glacial rebound rates in the Weddell Sea due to Late Holocene ice-sheet readvance, *Earth Planet. Sc.*
536 *Let.*, 413, 79-89, <https://doi.org/10.1016/j.epsl.2014.12.039>, 2015.
- 537 Bodart, J. A., Bingham, R. G., Ashmore, D. W., Karlsson, N.B., Hein, A. S., and Vaughan, D.
538 G.: Age-depth stratigraphy of Pine Island Glacier inferred from airborne radar and ice core
539 chronology, *J. Geophys. Res.-Earth*, 126, e2020JF005927, <https://doi.org/10.1029/2020JF005927>,
540 2021a.
- 541 Bodart, J.A., Bingham, R.G., Ashmore, D.W., Karlsson, N.B., Hein, A.S., and Vaughan,
542 D.G.: Dated radar stratigraphy of the Pine Island Glacier catchment (West Antarctica) derived from
543 BBAS-PASIN (2004-05) and OIB-MCoRDS2 (2016/2018) surveys, v.1.0.0, UK Polar Data Centre,
544 Natural Environment Research Council, UK Research and Innovation [data set],
545 <https://doi.org/10.5285/F2DE31AF-9F83-44F8-9584-F0190A2CC3EB>, 2021b.
- 546 Bodart, J.A.: Calculate WAIS Holocene accumulation from airborne radar reflector, v.1.0.0.,
547 Zenodo [code], doi TBD, 2023a.
- 548 Bodart, J.A., Bingham, R.G., Young, D.A., MacGregor, J.M., Ashmore, D.W., Quartini, E.,
549 Vaughan, D.G., and Blankenship D.D.: Gridded accumulation and depth products from dated airborne
550 radar stratigraphy over West Antarctica during the mid-Holocene, v.1.0.0, UK Polar Data Centre,
551 Natural Environment Research Council, UK Research and Innovation [data set], doi TBD, 2023b.
- 552 Buizert, C., Fudge, T.J., Roberts, W.H., Steig, E.J., Sherriff-Tadano, S., Ritz, C., Lefebvre, E.,
553 Edwards, J., Kawamura, K., Oyabu, I. and Motoyama, H.: Antarctic surface temperature and elevation
554 during the Last Glacial Maximum, *Science*, 372 (6546), 1097-1101,
555 <https://doi.org/10.1126/science.abd2897>, 2021.
- 556 Burgener, L., Rupper, S., Koenig, L., Forster, R., Christensen, W.F., Williams, J., Koutnik,
557 M., Mieke, C., Steig, E.J., Tingey, D. and Keeler, D.: An observed negative trend in West Antarctic



- 558 accumulation rates from 1975 to 2010: Evidence from new observed and simulated records. *J.*
559 *Geophys. Res.-Atmos.*, 118 (10), 4205-4216, <https://doi.org/10.1002/jgrd.50362>, 2013.
- 560 Cavitte, M.G., Blankenship, D.D., Young, D.A., Schroeder, D.M., Parrenin, F., Lemeur, E.,
561 Macgregor, J.A. and Siegert, M.J.: Deep radiostratigraphy of the East Antarctic plateau: connecting
562 the Dome C and Vostok ice core sites, *J. Glaciol.*, 62 (232), 323-334,
563 <https://doi.org/10.1017/jog.2016.11>, 2016.
- 564 Chavaillaz, Y., Codron, F. and Kageyama, M.: Southern westerlies in LGM and future
565 (RCP4.5) climates, *Clim. Past*, 9 (2), 517-524, <https://doi.org/10.5194/cp-9-517-2013>, 2013.
- 566 Cuffey, K.M., Clow, G.D., Steig, E.J., Buizert, C., Fudge, T.J., Koutnik, M., Waddington,
567 E.D., Alley, R.B. and Severinghaus, J.P.: Deglacial temperature history of West Antarctica, *P. Natl.*
568 *A. Sci.*, 113 (50), 14249-14254, <https://doi.org/10.1073/pnas.1609132113>, 2016.
- 569 Cole-Dai, J., Ferris, D.G., Kennedy, J.A., Sigl, M., McConnell, J.R., Fudge, T.J., Geng, L.,
570 Maselli, O.J., Taylor, K.C. and Souney, J.M.: Comprehensive record of volcanic eruptions in the
571 Holocene (11,000 years) from the WAIS Divide, Antarctica ice core, *J. Geophys. Res.-Atmos.*, 126
572 (7), p.e2020JD032855, <https://doi.org/10.1029/2020JD032855>, 2021.
- 573 Corr, H.F., Ferraccioli, F., Frearson, N., Jordan, T., Robinson, C., Armadillo, E., Caneva, G.,
574 Bozzo, E. and Tabacco, I.: Airborne radio-echo sounding of the Wilkes Subglacial Basin, the
575 Transantarctic Mountains and the Dome C region, *Terra Ant. Rep.*, 13, pp.55-63.
576 <https://nora.nerc.ac.uk/id/eprint/13578> (last access: 15 October 2022), 2007.
- 577 CReSIS: CReSIS Radar Depth Sounder Data, Lawrence, Kansas, USA. Digital Media.
578 <http://data.cresis.ku.edu/> (last access: 15 October 2022), 2018.
- 579 Dansgaard, W. and Johnsen, S. J.: A flow model and a time scale for the ice core from Camp
580 Century, Greenland, *J. Glacio.*, 8 (53), 215-223, <https://doi.org/10.3189/S0022143000031208>, 1969.
- 581 DeConto, R.M. and Pollard, D.: Contribution of Antarctica to past and future sea-level rise,
582 *Nature*, 531 (7596), 591-597, <https://doi.org/10.1038/nature17145>, 2016.
- 583 Denton, G.H. and Hughes, T.J.: Reconstructing the Antarctic ice sheet at the Last Glacial
584 Maximum, *Quaternary Sci. Rev.*, 21 (1-3), 193-202, [https://doi.org/10.1016/S0277-3791\(01\)00090-7](https://doi.org/10.1016/S0277-3791(01)00090-7),
585 2002.
- 586 Fahnstock, M., Abdalati, W., Joughin, I., Brozena, J. and Gogineni, P.: High geothermal heat
587 flow, basal melt, and the origin of rapid ice flow in central Greenland, *Science*, 294 (5550), 2338-
588 2342, <https://doi.org/10.1126/science.1065370>, 2001.
- 589 Favier, V., Agosta, C., Parouty, S., Durand, G., Delaygue, G., Gallée, H., Drouet, A.-S.,
590 Trouvilliez, A., and Krinner, G.: An updated and quality controlled surface mass balance dataset for
591 Antarctica, *The Cryosphere*, 7, 583-597, <https://doi.org/10.5194/tc-7-583-2013>, 2013.
- 592 Frémand, A.C., Bodart, J.A., Jordan, T.A., Ferraccioli, F., Robinson, C., Corr, H.F., Peat,
593 H.J., Bingham, R.G. and Vaughan, D.G.: British Antarctic Survey's Aerogeophysical Data: Releasing
594 25 Years of Airborne Gravity, Magnetic, and Radar Datasets over Antarctica, *Earth Syst. Sci. Data*,
595 14, 3379-3410, <https://doi.org/10.5194/essd-14-3379-2022>, 2022.
- 596 Fudge, T.J., Markle, B.R., Cuffey, K.M., Buizert, C., Taylor, K.C., Steig, E.J., Waddington,
597 E.D., Conway, H. and Koutnik, M.: Variable relationship between accumulation and temperature in
598 West Antarctica for the past 31,000 years, *Geophys. Res. Lett.*, 43(8), 3795-3803,
599 <https://doi.org/10.1002/2016GL068356>, 2016.



- 600 Fudge, T. J., Buizert, C., Conway, H., and Waddington, E. D.: Accumulation Rates from the
601 WAIS Divide Ice Core, v.1.0.0., U.S. Antarctic Program Data Center [data set],
602 <https://doi.org/10.15784/601004>, 2017.
- 603 Haran, T., M. Klinger, J. Bohlander, M. Fahnestock, T. Painter, and T. Scambos: MEaSUREs
604 MODIS Mosaic of Antarctica 2013-2014 (MOA2014) Image Map, v.1.0.0., NASA National Snow
605 and Ice Data Center Distributed Active Archive Center [data set],
606 <https://doi.org/10.5067/RNF17BP824UM>, 2018.
- 607 Harrison, C. H.: Radio Echo Sounding of Horizontal Layers in Ice, *J. Glaciol.*, 12, 66, 383–
608 397, <https://doi.org/10.3189/S0022143000031804>, 1973.
- 609 Hein, A.S., Marrero, S.M., Woodward, J., Dunning, S.A., Winter, K., Westoby, M.J.,
610 Freeman, S.P., Shanks, R.P. and Sugden, D.E.: Mid-Holocene pulse of thinning in the Weddell Sea
611 sector of the West Antarctic ice sheet, *Nat. Commun.*, 7 (1), 1-8,
612 <https://doi.org/10.1038/ncomms12511>, 2016.
- 613 Hillenbrand, C.D., Kuhn, G., Smith, J.A., Gohl, K., Graham, A.G., Larter, R.D., Klages, J.P.,
614 Downey, R., Moreton, S.G., Forwick, M. and Vaughan, D.G.: Grounding-line retreat of the west
615 Antarctic ice sheet from inner Pine island Bay, *Geology*, 41 (1), 35-38,
616 <https://doi.org/10.1130/G33469.1>, 2013.
- 617 Hillenbrand, C.D., Bentley, M.J., Stollendorf, T.D., Hein, A.S., Kuhn, G., Graham, A.G.,
618 Fogwill, C.J., Kristoffersen, Y., Smith, J.A., Anderson, J.B. and Larter, R.D.: Reconstruction of
619 changes in the Weddell Sea sector of the Antarctic Ice Sheet since the Last Glacial Maximum,
620 *Quaternary Sci. Rev.*, 100, 111-136, <https://doi.org/10.1016/j.quascirev.2013.07.020>, 2014.
- 621 Hillenbrand, C.D., Smith, J.A., Hodell, D.A., Greaves, M., Poole, C.R., Kender, S., Williams,
622 M., Andersen, T.J., Jernas, P.E., Elderfield, H. and Klages, J.P.: West Antarctic Ice Sheet retreat
623 driven by Holocene warm water incursions, *Nature*, 547 (7661), 43-48,
624 <https://doi.org/10.1038/nature22995>, 2017.
- 625 Holt, J. W., Blankenship, D. D., Morse, D. L., Young, D. A., Peters, M. E., Kempf, S. D.,
626 Richter, T. G., Vaughan, D. G., and Corr, H. F.: New boundary conditions for the West Antarctic Ice
627 Sheet: Subglacial topography of the Thwaites and Smith glacier catchments, *Geophys. Res. Lett.*, 33,
628 L09502, <https://doi.org/10.1029/2005GL025561>, 2006.
- 629 IPCC: Climate Change 2021: The Physical Science Basis. Contribution of Working Group I
630 to the Sixth Assessment Report of the Intergovernmental Panel on Climate Change, edited by:
631 Masson-Delmotte, V., Zhai, P., Pirani, A., Connors, S. L., Péan, C., Berger, S., Caud, N., Chen, Y.,
632 Goldfarb, L., Gomis, M. I., Huang, M., Leitzell, K., Lonnoy, E., Matthews, J. B. R., Maycock, T. K.,
633 Waterfield, T., Yelekçi, O., Yu, R., and Zhou B., Cambridge University Press, Cambridge, United
634 Kingdom and New York, NY, USA, 147–286, <https://doi.org/10.1017/9781009157896.003>, in press,
635 2021.
- 636 Jacobel, R. W., and Welch, B. C.: A time marker at 17.5 kyr BP detected throughout West
637 Antarctica, *Ann. Glaciol.*, 41, 47–51, <https://doi.org/10.3189/172756405781813348>, 2005.
- 638 Johnson, J.S., Bentley, M.J., Smith, J.A., Finkel, R.C., Rood, D.H., Gohl, K., Balco, G.,
639 Larter, R.D. and Schaefer, J.M.: Rapid thinning of Pine Island Glacier in the early Holocene, *Science*,
640 343 (6174), 999-1001, <https://doi.org/10.1126/science.1247385>, 2014.
- 641 Johnson, J.S., Roberts, S.J., Rood, D.H., Pollard, D., Schaefer, J.M., Whitehouse, P.L.,
642 Ireland, L.C., Lamp, J.L., Goehring, B.M., Rand, C. and Smith, J.A.: Deglaciation of Pope Glacier



- 643 implies widespread early Holocene ice sheet thinning in the Amundsen Sea sector of Antarctica, *Earth*
644 *Planet Sc. Lett.*, 548, p.116501, <https://doi.org/10.1016/j.epsl.2020.116501>, 2020.
- 645 Johnson, J.S., Pollard, D., Whitehouse, P.L., Roberts, S.J., Rood, D.H. and Schaefer, J.M.:
646 Comparing glacial-geological evidence and model simulations of ice sheet change since the last
647 glacial period in the Amundsen Sea sector of Antarctica, *J. Geophys. Res.-Earth*, 126(6),
648 p.e2020JF005827, <https://doi.org/10.1029/2020JF005827>, 2021.
- 649 Johnson, J.S., Venturelli, R.A., Balco, G., Allen, C.S., Braddock, S., Campbell, S., Goehring,
650 B.M., Hall, B.L., Neff, P.D., Nichols, K.A. and Rood, D.H.: Existing and potential evidence for
651 Holocene grounding line retreat and readvance in Antarctica, *The Cryosphere*, 16 (5), 1543-1562,
652 <https://doi.org/10.5194/tc-16-1543-2022>, 2022.
- 653 Jones, R.S., Johnson, J.S., Lin, Y., Mackintosh, A.N., Sefton, J.P., Smith, J.A., Thomas, E.R.
654 and Whitehouse, P.L.: Stability of the Antarctic Ice Sheet during the pre-industrial Holocene, *Nat.*
655 *Rev. Earth Environ.*, 3, 500-515, <https://doi.org/10.1038/s43017-022-00309-5>, 2022.
- 656 Karlsson, N. B., Bingham, R. G., Rippin, D. M., Hindmarsh, R. C., Corr, H. F., and Vaughan,
657 D. G.: Constraining past accumulation in the central Pine Island Glacier basin, West Antarctica, using
658 radio-echo sounding, *J. Glaciol.*, 60, 553–562, <https://doi.org/10.3189/2014JG13j180>, 2014.
- 659 Kingslake, J., Scherer, R.P., Albrecht, T., Coenen, J., Powell, R.D., Reese, R., Stansell, N.D.,
660 Tulaczyk, S., Wearing, M.G. and Whitehouse, P.L.: Extensive retreat and re-advance of the West
661 Antarctic Ice Sheet during the Holocene, *Nature*, 558 (7710), 430-434,
662 <https://doi.org/10.1038/s41586-018-0208-x>, 2018.
- 663 Koutnik, M.R., Fudge, T.J., Conway, H., Waddington, E.D., Neumann, T.A., Cuffey, K.M.,
664 Buizert, C. and Taylor, K.C.: Holocene accumulation and ice flow near the West Antarctic Ice Sheet
665 Divide ice core site, *J. Geophys. Res.-Earth*, 121 (5), 907-924. <https://doi.org/10.1002/2015JF003668>,
666 2016.
- 667 Kurbatov, A.V., Zielinski, G.A., Dunbar, N.W., Mayewski, P.A., Meyerson, E.A., Sneed,
668 S.B. and Taylor, K.C.: A 12,000 year record of explosive volcanism in the Siple Dome Ice Core, West
669 Antarctica, *J. Geophys. Res.-Atmos*, 111 (D12). <https://doi.org/10.1029/2005JD006072>, 2006.
- 670 Leysinger Vieli, G.J.M., Hindmarsh, R.C., Siegert, M.J. and Bo, S.: Time-dependence of the
671 spatial pattern of accumulation rate in East Antarctica deduced from isochronic radar layers using a 3-
672 D numerical ice flow model, *J. Geophys. Res.-Earth*, 116 (F2), F02018,
673 <https://doi.org/10.1029/2010JF001785>, 2011.
- 674 MacGregor, J.A., Matsuoka, K., Koutnik, M.R., Waddington, E.D., Studinger, M. and
675 Winebrenner, D.P.: Millennially averaged accumulation rates for the Vostok Subglacial Lake region
676 inferred from deep internal layers, *Ann. Glaciol.*, 50 (51), 25-34.
677 <https://doi.org/10.3189/172756409789097441>, 2009.
- 678 MacGregor, J.A., Catania, G.A., Conway, H., Schroeder, D.M., Joughin, I., Young, D.A.,
679 Kempf, S.D. and Blankenship, D.D.: Weak bed control of the eastern shear margin of Thwaites
680 Glacier, West Antarctica, *J. Glaciol.*, 59 (217), 900-912, <https://doi.org/10.3189/2013JG13J050>,
681 2013.
- 682 MacGregor, J. A., Colgan, W. T., Fahnestock, M. A., Morlighem, M., Catania, G. A., Paden,
683 J. D., and Gogineni, S. P.: Holocene deceleration of the Greenland ice sheet, *Science*, 351 (6273),
684 590–593, <https://doi.org/10.1126/science.aab1702>, 2016.
- 685 MacGregor, J. A., Boisvert, L. N., Medley, B., Petty, A. A., Harbeck, J. P., Bell, R. E., Blair,
686 J. B., Blanchard-Wrigglesworth, E., Buckley, E.,M., Christoffersen, M. S., and Cochran, J. R.: The



- 687 scientific legacy of NASA's Operation Icebridge, *Rev. Geophys.*, 59, e2020RG000712,
688 <https://doi.org/10.1029/2020RG000712>, 2021.
- 689 Mayewski, P. A. and Dixon, D.A.: US International TransAntarctic Scientific Expedition (US
690 ITASE) Glaciochemical Data, v. 2.0.0., NASA National Snow and Ice Data Center [data set],
691 <http://dx.doi.org/10.7265/N51V5BXR>, 2013.
- 692 McConnell, J.R., Burke, A., Dunbar, N.W., Köhler, P., Thomas, J.L., Arienzo, M.M.,
693 Chellman, N.J., Maselli, O.J., Sigl, M., Adkins, J.F. and Baggenstos, D.: Synchronous volcanic
694 eruptions and abrupt climate change~ 17.7 ka plausibly linked by stratospheric ozone depletion, *P.*
695 *Natl. A. Sci.*, 114 (38), 10035-10040, <https://doi.org/10.1073/pnas.1705595114>, 2017.
- 696 Medley, B., Joughin, I., Das, S.B., Steig, E.J., Conway, H., Gogineni, S., Criscitiello, A.S.,
697 McConnell, J.R., Smith, B.E., van den Broeke, M.R. and Lenaerts, J.T.: Airborne-radar and ice-core
698 observations of annual snow accumulation over Thwaites Glacier, West Antarctica confirm the
699 spatiotemporal variability of global and regional atmospheric models, *Geophys. Res. Lett.*, 40(14),
700 pp.3649-3654, <https://doi.org/10.1002/grl.50706>, 2013.
- 701 Medley, B., Joughin, I., Smith, B.E., Das, S.B., Steig, E.J., Conway, H., Gogineni, S., Lewis,
702 C., Criscitiello, A.S., McConnell, J.R. and van den Broeke, M.R.: Constraining the recent mass
703 balance of Pine Island and Thwaites glaciers, West Antarctica, with airborne observations of snow
704 accumulation, *The Cryosphere*, 8 (4), 1375-1392, <https://doi.org/10.5194/tc-8-1375-2014>, 2014.
- 705 Morlighem, M.: MEaSURES BedMachine Antarctica, v.2.0.0., NASA National Snow and Ice
706 Data Center Distributed Active Archive Center [data set], <https://doi.org/10.5067/E1QL9HFQ7A8M>,
707 2020.
- 708 Mouginit, J., Scheuchl, B., and Rignot., E.: MEaSURES Antarctic Boundaries for IPY 2007-
709 2009 from Satellite Radar, v.2.0.0., NASA National Snow and Ice Data Center Distributed Active
710 Archive Center [data set], <http://dx.doi.org/10.5067/AXE4121732AD>, 2017.
- 711 Muldoon, G. R., Jackson, C. S., Young, D. A., and Blankenship, D. D.: Bayesian estimation
712 of englacial radar chronology in Central West Antarctica, *Dynamics and Statistics of the Climate*
713 *System*, 3(1), dzy004, <https://doi.org/10.1093/climatesystem/dzy004>, 2018.
- 714 Neuhaus, S.U., Tulaczyk, S.M., Stansell, N.D., Coenen, J.J., Scherer, R.P., Mikucki, J.A. and
715 Powell, R.D.: Did Holocene climate changes drive West Antarctic grounding line retreat and
716 readvance?, *The Cryosphere*, 15(10), 4655-4673, <https://doi.org/10.5194/tc-15-4655-2021>, 2021.
- 717 Neumann, T. A., Conway, H., Price, S. F., Waddington, E. D., Catania, G. A., and Morse, D.
718 L.: Holocene accumulation and ice sheet dynamics in central West Antarctica, *J. Geophys. Res.-Earth*,
719 113 (F2), F02018, <https://doi.org/10.1029/2007JF000764>, 2008.
- 720 Nichols, K.A., Goehring, B.M., Balco, G., Johnson, J.S., Hein, A.S. and Todd, C.: New last
721 glacial maximum ice thickness constraints for the Weddell Sea Embayment, Antarctica, *The*
722 *Cryosphere*, 13(11), 2935-2951, <https://doi.org/10.5194/tc-13-2935-2019>, 2019.
- 723 Nye, J. F.: The distribution of stress and velocity in glaciers and ice-sheets, *P. Roy. Soc.*
724 *Lond. A. Mat.*, 239 (1216), 113-133. <https://doi.org/10.1098/rspa.1957.0026>, 1957.
- 725 Peters, M.E., Blankenship, D.D., Carter, S.P., Kempf, S.D., Young, D.A. and Holt, J.W.:
726 Along-track focusing of airborne radar sounding data from West Antarctica for improving basal
727 reflection analysis and layer detection, *IEEE T. Geosci. Remote.*,
728 <https://doi.org/10.1109/TGRS.2007.897416>, 45 (9), 2725-2736, 2007.



- 729 Rignot, E., Mouginot, J., and Scheuchl, B.: MEaSURES InSAR-based Antarctica ice velocity
730 map, v.2.0.0., NASA National Snow and Ice Data Center Distributed Active Archive Center [data
731 set], <https://doi.org/10.5067/D7GK8F5J8M8R>, 2017.
- 732 Ross, N., Siegert, M.J., Woodward, J., Smith, A.M., Corr, H.F., Bentley, M.J., Hindmarsh,
733 R.C., King, E.C. and Rivera, A.: Holocene stability of the Amundsen-Weddell ice divide, West
734 Antarctica, *Geology*, 39 (10), 935-938, <https://doi.org/10.1130/G31920.1>, 2011.
- 735 Ross, N., Bingham, R.G., Corr, H.F., Ferraccioli, F., Jordan, T.A., Le Brocq, A., Rippin,
736 D.M., Young, D., Blankenship, D.D. and Siegert, M.J.: Steep reverse bed slope at the grounding line
737 of the Weddell Sea sector in West Antarctica, *Nat. Geosci.*, 5 (6), 393-396,
738 <https://doi.org/10.1038/ngeo1468>, 2012.
- 739 Siegert, M.J. and Payne, A.J.: Past rates of accumulation in central West Antarctica, *Geophys.*
740 *Res. Lett.*, 31 (12), <https://doi.org/10.1029/2004GL020290>, 2004.
- 741 Siegert, M., Ross, N., Corr, H., Kingslake, J. and Hindmarsh, R.: Late Holocene ice-flow
742 reconfiguration in the Weddell Sea sector of West Antarctica, *Quaternary Sci. Rev.*, 78, 98-107,
743 <https://doi.org/10.1016/j.quascirev.2013.08.003>, 2013.
- 744 Sigl, M., Toohey, M., McConnell, J.R., Cole-Dai, J., and Severi, M.: Volcanic stratospheric
745 sulfur injections and aerosol optical depth during the Holocene (past 11 500 years) from a bipolar ice-
746 core array, *Earth Syst. Sci.*, 14, 3167–3196, <https://doi.org/10.5194/essd-14-3167-2022>, 2022.
- 747 Spector, P., Stone, J. and Goehring, B.: Thickness of the divide and flank of the West
748 Antarctic Ice Sheet through the last deglaciation, *The Cryosphere*, 13 (11), 3061-3075,
749 <https://doi.org/10.5194/tc-13-3061-2019>, 2019.
- 750 Sproson, A.D., Yokoyama, Y., Miyairi, Y., Aze, T. and Totten, R.L.: Holocene melting of the
751 West Antarctic Ice Sheet driven by tropical Pacific warming, *Nat. Commun.*, 13 (1), 1-9,
752 <https://doi.org/10.1038/s41467-022-30076-2>, 2022.
- 753 Steig, E.J., Fastook, J.L., Zweck, C., Goodwin, I.D., Licht, K.J., White, J.W. and Ackert Jr,
754 R.P.: West Antarctic ice sheet elevation changes, *The West Antarctic Ice Sheet: Behavior and*
755 *Environment*, 77, 75-90. <https://doi.org/10.1029/AR077p0075>, 2001.
- 756 Stone, J.O., Balco, G.A., Sugden, D.E., Caffee, M.W., Sass III, L.C., Cowdery, S.G. and
757 Siddoway, C.: Holocene deglaciation of Marie Byrd land, west Antarctica, *Science*, 299 (5603), 99-
758 102, <https://doi.org/10.1126/science.1077998>, 2003.
- 759 Sutter, J., Fischer, H. and Eisen, O.: Investigating the internal structure of the Antarctic ice
760 sheet: the utility of isochrones for spatiotemporal ice-sheet model calibration, *The Cryosphere*, 15 (8),
761 3839-3860. <https://doi.org/10.5194/tc-15-3839-2021>, 2021.
- 762 Van Den Broeke, M.R. and Van Lipzig, N.P.: Changes in Antarctic temperature, wind and
763 precipitation in response to the Antarctic Oscillation, *Ann. Glaciol.*, 39, 119-126,
764 <https://doi.org/10.3189/172756404781814654>, 2004.
- 765 Van Wessem, J.M., Van De Berg, W.J., Noël, B.P., Van Meijgaard, E., Amory, C., Birnbaum,
766 G., Jakobs, C.L., Krüger, K., Lenaerts, J., Lhermitte, S. and Ligtenberg, S.R.: Modelling the climate
767 and surface mass balance of polar ice sheets using RACMO2–Part 2: Antarctica (1979–2016), *The*
768 *Cryosphere*, 12 (4), 479-1498, <https://doi.org/10.5194/tc-12-1479-2018>, 2018.
- 769 Vaughan, D.G., Corr, H.F., Ferraccioli, F., Frearson, N., O'Hare, A., Mach, D., Holt, J.W.,
770 Blankenship, D.D., Morse, D.L. and Young, D.A.: New boundary conditions for the West Antarctic



- 771 ice sheet: Subglacial topography beneath Pine Island Glacier, *Geophys. Res. Lett.*, 33 (9), L09501,
772 <https://doi.org/10.1029/2005GL025588>, 2006.
- 773 Venturelli, R.A., Siegfried, M.R., Roush, K.A., Li, W., Burnett, J., Zook, R., Fricker, H.A.,
774 Priscu, J.C., Leventer, A. and Rosenheim, B.E.: Mid-Holocene grounding line retreat and readvance
775 at Whillans Ice Stream, West Antarctica, *Geophys. Res. Lett.*, 47 (15), p.e2020GL088476,
776 <https://doi.org/10.1029/2020GL088476>, 2020.
- 777 Waddington, E. D., Neumann, T. A., Koutnik, M. R., Marshall, H.-P., and Morse, D. L.:
778 Inference of accumulation-rate patterns from deep layers in glaciers and ice sheets, *J. Glaciol.*, 53
779 (183), 694–712, <https://doi.org/10.3189/002214307784409351>, 2007.
- 780 WAIS Divide Project Members: Onset of deglacial warming in West Antarctica driven by
781 local orbital forcing, *Nature*, 500 (7463), 440–444, <https://doi.org/10.1038/nature12376>, 2013.
- 782 Wearing, M.G. and Kingslake, J.: Holocene Formation of Henry Ice Rise, West Antarctica,
783 Inferred from Ice-Penetrating Radar, *J. Geophys. Res.-Earth*, 124 (8), 2224–2240,
784 <https://doi.org/10.1029/2018JF004988>, 2019.
- 785 Whillans, I. M.: Radio-echo layers and the recent stability of the West Antarctic ice sheet,
786 *Nature*, 264, 5582, 152, <https://doi.org/10.1038/264152a0>, 1976.
- 787 Winter, A., Steinhage, D., Creyts, T.T., Kleiner, T. and Eisen, O.: Age stratigraphy in the East
788 Antarctic Ice Sheet inferred from radio-echo sounding horizons, *Earth Syst. Sci. Data*, 11 (3), 1069-
789 1081, <https://doi.org/10.5194/essd-11-1069-2019>, 2019.